



## Full length article

# In-situ and ex-situ microstructure studies and dislocation-based modelling for primary creep regeneration response of 316H stainless steel

X. Li<sup>a,b</sup>, S.R. Holdsworth<sup>a</sup>, S. Kalácska<sup>c</sup>, L. Balogh<sup>d</sup>, J. -S Park<sup>e</sup>, Y. Arroyo Rojas Dasilva<sup>a</sup>, X. Maeder<sup>c</sup>, A. Cocks<sup>f</sup>, E. Mazza<sup>a,b</sup>, E. Hosseini<sup>a,\*</sup>

<sup>a</sup> Empa, Swiss Federal Laboratories for Material Science and Technology, Überlandstrasse 129, CH-8600 Dübendorf, Switzerland

<sup>b</sup> ETH Zürich, Institute for Mechanical Systems, Department of Mechanical and Process Engineering, 8092 Zürich, Switzerland

<sup>c</sup> Empa, Swiss Federal Laboratories for Materials Science and Technology, Feuerwerkerstrasse 39, CH-3602 Thun, Switzerland

<sup>d</sup> Queen's University, Department of Mechanical and Materials Engineering, Kingston, ON K7L 3N6, Canada

<sup>e</sup> Argonne National Laboratory, X-ray Science Division, Lemont, IL 60439, USA

<sup>f</sup> University of Oxford, Department of Engineering Science, Parks Road, Oxford OX1 3PJ, UK

## ARTICLE INFO

## Article history:

Received 5 March 2021

Revised 22 June 2021

Accepted 22 June 2021

Available online 27 June 2021

## Keywords:

Primary creep regeneration

Dislocation-based model

In-situ synchrotron XRD

Neutron diffraction

TEM

EBS

316H austenitic steel

## ABSTRACT

The emergence of renewable energy sources with their variable and unpredictable nature, in addition to the variation of energy need for weekdays vs. weekends, demands an ever flexible operation of thermal power plants. Such a feature has therefore altered the typical steady creep loading of high-temperature components of power plants to stress-varying or cyclic creep conditions. The introduced load transients have been found to affect the strain hardening memory of the creeping alloys and might lead to multiple primary creep regeneration (PCR). Therefore, the creep strain accumulation can considerably increase under such conditions. Consideration of the PCR phenomenon is beyond the capability of conventional creep constitutive models which are based on strain- or time-hardening assumptions. The present study conducted *in-situ* and *ex-situ* experiments for 316H stainless steel. Various microstructural examination techniques, such as synchrotron high energy X-ray and neutron diffraction, and backscattered and transmission electron microscopy, have been employed for characterising evolution of the dislocation structure and the internal lattice strain/stress state of the alloy during stress-varying and cyclic creep conditions. The formation/annihilation of dislocation pileups and the bowing/unbowing of dislocation-lines were identified as the responsible mechanisms for PCR. A dislocation-based model was then formulated which could well represent the measured microstructural evolution and mechanical response of the steel during the conducted experiments at 650°C.

© 2021 The Author(s). Published by Elsevier Ltd on behalf of Acta Materialia Inc.

This is an open access article under the CC BY license (<http://creativecommons.org/licenses/by/4.0/>)

## 1. Introduction

In a creeping alloy, a load reversal may clear the previous hardening memory, and lead to a period of high creep strain rates upon reloading, i.e. primary creep regeneration (PCR) is seen. The experimental observations from a set of stress-varying creep tests showed that the extent of PCR activation is sensitive to the reverse-loading conditions and is generally more significant for larger magnitudes and longer durations of reverse-loading [1–3].

This study aims to provide a mechanistic description of the PCR phenomenon in 316H steel.

A series of *in-situ* and *ex-situ* stress-varying creep experiments have been conducted for the 316H steel at 650°C. Employment of different microstructural characterisation techniques allowed tracking the evolution trends of dislocation structure and internal strain/stress and accordingly provided a reliable understanding of the responsible mechanisms of PCR. Similarly, a recent study in Bristol [4] employed *in-situ* neutron diffraction and proposed that the activation of PCR is related to the accumulation of residual lattice strains during the reverse plastic loading. The employment of additional microstructural characterisation techniques in the present study could provide a deeper understanding of the PCR phenomenon. Accordingly, a mechanistic dislocation-based model

\* Corresponding author at: High Temperature Integrity Group (HTIG), EMPA, Swiss Federal Laboratories for Materials Science and Technology, Switzerland.

E-mail address: [ehsan.hosseini@empa.ch](mailto:ehsan.hosseini@empa.ch) (E. Hosseini).

has been developed for representing the evolution of microstructural parameters and creep strain response of the alloy during stress-varying creep loading. A previous study by Petkov et al. [5] proposed a dislocation-based model representing the creep response of 316H steel under stress-varying creep conditions. Although the model could reasonably predict the results of their mechanical experiments, it could not interpret the experimentally observed dislocation density evolution during the conducted *in-situ* and *ex-situ* stress-varying creep experiments in this study, which indicated a need for further elaboration of the model assumptions and formulations.

The structure of the paper is as follows. Section 2 presents the *ex-situ* and *in-situ* experimental techniques and results. Section 3 discusses the experimental observations to understand the responsible mechanism(s) of PCR. Finally, section 4 formulates a dislocation-based model based on the identified mechanisms for PCR and compares the model outcomes with the measured microstructure and strain evolution during the conducted experiments.

## 2. Experiments

This section presents details of the conducted *ex-situ* and *in-situ* experiments for the 316H stainless steel. The examined 316H alloy originated from an EDF (Électricité de France) ex-service turbine steam-header (operated 90,930 h at ~520°C) and had a chemical composition of 17.1%Cr, 11.4%Ni, 2.3%Mo, 1.0%Mn and 0.07%C (wt. %). This EDF steel is the same as that previously investigated in Oxford [5–8], Bristol [9] and Open university [10,11]. This study presents a detailed description of the PCR phenomenon for the steel and provides a basis for proposing guidelines which can realistically consider PCR in EDF's R5 high temperature mechanical assessment procedure.

### 2.1. Ex-situ experiment

The *ex-situ* investigation included seven interrupted creep experiments and aimed to create microstructurally representative samples at different states of a stress-varying creep loading profile at 650°C (Fig. 1a). The dislocation structure and internal lattice strain/stress of the generated samples were then characterised by neutron diffraction (ND), transmission electron microscopy (TEM) and electron backscatter diffraction (EBSD). The outcomes of previously conducted experiments in [1,3] were explored to design the *ex-situ* loading profile such that a trivial and significant PCR would be observed after reloading to states 5 and 7, respectively. The employed setup and procedure for the *ex-situ* tests are identical to those comprehensively described in [12].

It should be noted that comparing the creep deformation behaviour of different samples indicated a non-negligible specimen-to-specimen variability for the examined 316H alloy (Fig. 1b) which calls for caution in interpretation of the experimental observations from the *ex-situ* study. As the investigated alloy originated from an ex-service component, different specimen source locations could have been subjected to different thermo-mechanical histories during operation, which could likely account for the observed specimen-to-specimen variability. Such a specimen-to-specimen variability was also observed by [5,8] where the same alloy was investigated.

#### 2.1.1. Neutron diffraction

The ENGIX neutron diffractometer at the ISIS facility (Oxfordshire, UK) was used for gathering diffraction data for the ND samples (Fig. 1a inset). Six crystallographic plane families of {111}, {200}, {220}, {311}, {222} and {400} were evaluated for calculation of the internal lattice strain and dislocation density. During

the measurements, the normal directions of these plane families were parallel to the specimen's axial direction (i.e. loading direction).

#### Internal lattice strain

Lattice strain of crystallographic planes is calculated as:

$$\varepsilon_{hkl}^* = \frac{d_{hkl}^* - d_{hkl}^0}{d_{hkl}^0} \quad (1)$$

where  $d_{hkl}^0$  is the lattice spacing for the {hkl} plane measured for specimen E1 and  $d_{hkl}^*$  is the lattice spacing for samples E2–7. As can be seen in Fig. 2a and similar to the observations in [13], the lower lattice elastic moduli for {200} and {400} planes led to larger internal lattice strain magnitudes which therefore are less affected by the noise/scatter of the measurements. In the absence of reliable internal lattice strain measurements for the specimen's radial direction, calculation of internal stress was not feasible. Therefore, internal lattice strains in the loading direction were considered as indicators for the internal stress.

Fig 2b shows that the internal lattice strain gradually formed and increased during forward-loading (E1→E3). Reverse-loading relaxed the generated internal lattice strains and resulted in internal lattice strains with the opposite direction/sign (E3→E4 and E4→E6). Forward reloading (E4→E5 and E6→E7) relaxed the internal lattice strains formed during the reverse-loading. Comparing the internal lattice strains of samples E5 and E7 with that of sample E3 indicates that the longer reverse-loading imposed a larger change of the alloy's internal lattice strain/stress.

#### Dislocation density

The Convolutional Multiple Whole Profile (CMWP) [14–20] method was employed to evaluate diffraction patterns and calculate the evolution of dislocation density. The output of the CMWP method typically includes five microstructural parameters; namely mean  $m$  and variance  $\sigma$  of the log-normal size distribution of equiaxed coherently-scattering-domains, dislocation density  $\rho$ , variable  $q$  describing the edge/screw dislocation ratio, and dimensionless variable  $M^*$  defining the dislocation arrangement (readers are referred to [21–23] for more detailed information). The CMWP analysis focused on the determination of the variation of dislocation density  $\rho$ , and negligible variation for  $m$ ,  $\sigma$ ,  $q$  and  $M^*$  is assumed. Since the derived dislocation density values are small and at the technique's reliability limit, interpretation of the observations will focus on the evolution trends rather than the derived dislocation densities. Fig. 3 shows that the dislocation density increased during the initial forward-loading (E1→E3), dropped upon reverse-loading (E3→E4) and increased again after reloading during transitions E4→E5 and E6→E7. Interestingly, one hour reverse-loading increased the dislocation density (E4→E6).

#### 2.1.2. Transmission electron microscopy

Mechanical grinding, polishing and electropolishing using A2 Struers® solution at –3°C were employed to prepare TEM thin foils. For the sake of consistency, bright-field (BF) images were taken for all the samples under  $g = [111]$  two-beam conditions (Figs. 4b–h). The 'grid-intercept method' was employed for calculating dislocation density from the TEM images [24,25] (e.g. Fig. 4a):

$$\rho = \frac{1}{t} \frac{\sum_{i=1}^N \left( \frac{n_i}{L_i} \right)}{N} \quad (2)$$

where  $t$  is the thickness of the TEM foil (~186 nm, estimated from convergent electron beam diffraction under two-beam conditions);  $n_i$  is the number of intersections between  $i^{\text{th}}$  grid line and dislocations;  $L$  is the length of  $i^{\text{th}}$  grid line, and  $N$  is the number of grid lines. At least, 20 micrographs from different areas were analysed for calculating the average dislocation density for each sample of

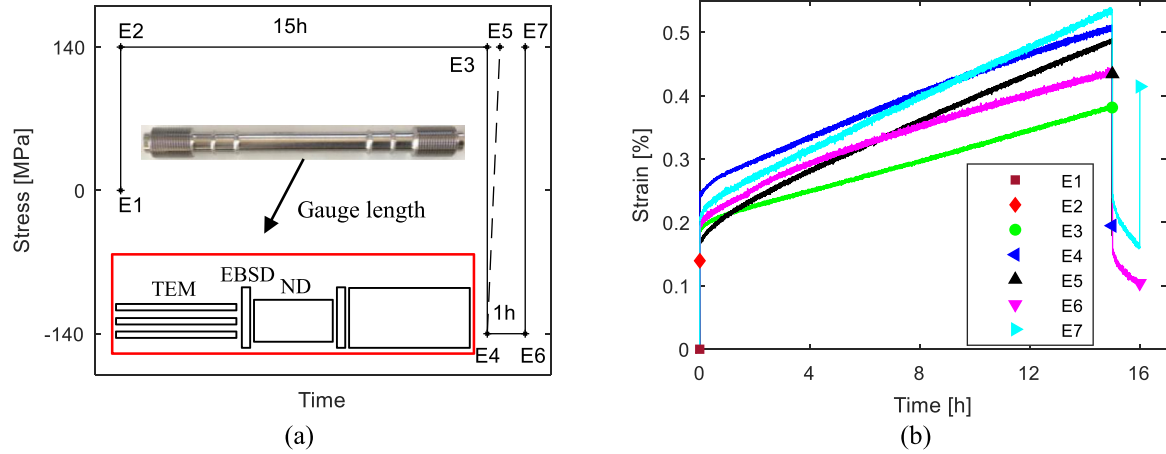


**Fig. 1.** Designed loading profile for the *ex-situ* experiments for the 316H steel at 650°C (a), and the observed deformation response for the examined samples (b).

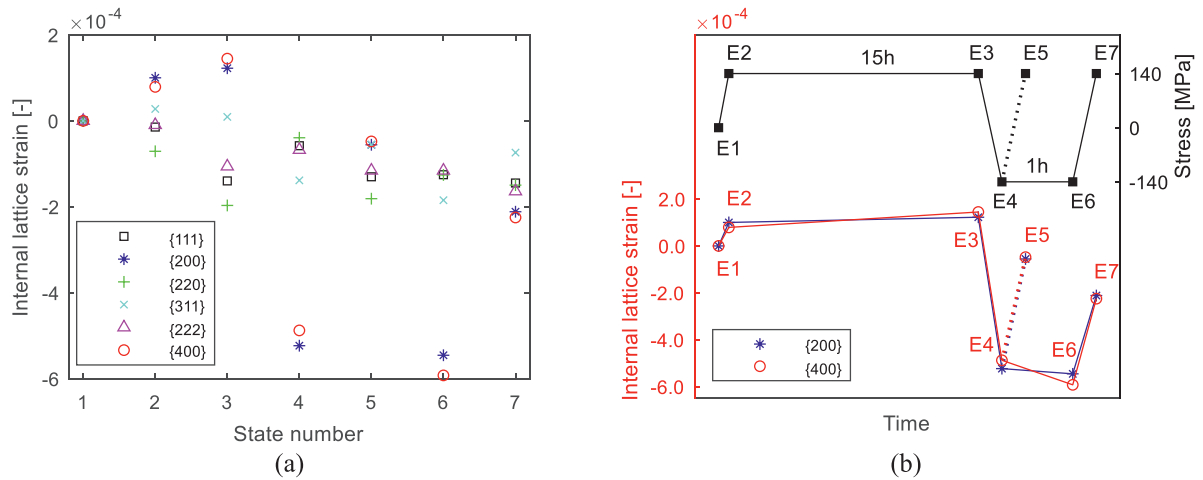


**Fig. 2.** Axial internal lattice strains for six planes of the samples from the *ex-situ* experiment (a), and internal strain evolution for {200} and {400} planes for the *ex-situ* loading profile (b).

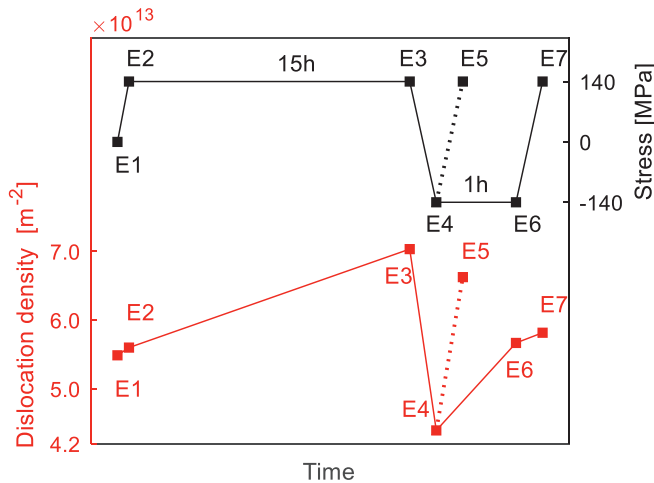


**Fig. 3.** CMWP derived dislocation density evolution for the *ex-situ* loading profile.

the *ex-situ* experiment. As shown in Fig. 4i, the observed evolution trend for the dislocation density is comparable to that derived from the ND examinations (Fig. 3).

### 2.1.3. Electron backscatter diffraction

Geometrically necessary dislocation (GND) densities were evaluated using kernel average misorientation (KAM) values derived from EBSD measurements [26,27]. Fig. 5 illustrates an example of the inverse pole figure (IPF), GND maps for the seven examined samples and accordingly, the evolution of average GND density for the *ex-situ* loading profile.

It can be seen from Fig. 5 that the GND population (unexpectedly) decreased during initial loading (E1→E2), and subsequently increased during the 15 h forward-loading (E2→E3). Reverse-loading reduced the GND density (E3→E4), while the drop was partially recovered upon reloading (E4→E5). Interestingly, 1 h reverse-loading (E4→E6) and subsequent reloading (E6→E7) increased and decreased the GND density, respectively. The evolution trend of GND density and other derived microstructural parameters are further discussed in Section 3.

### 2.2. In-situ experiment

The *ex-situ* study combined different microstructural examination techniques on seven different specimens. The gathered microstructural evidence showed that the PCR phenomenon is related to the evolution of dislocation structure and internal lattice strain during stress-varying creep loading. To assure that the derived conclusions will not be affected by the observed specimen-to-specimen variability (see Fig. 1b), a high-temperature *in-situ* syn-



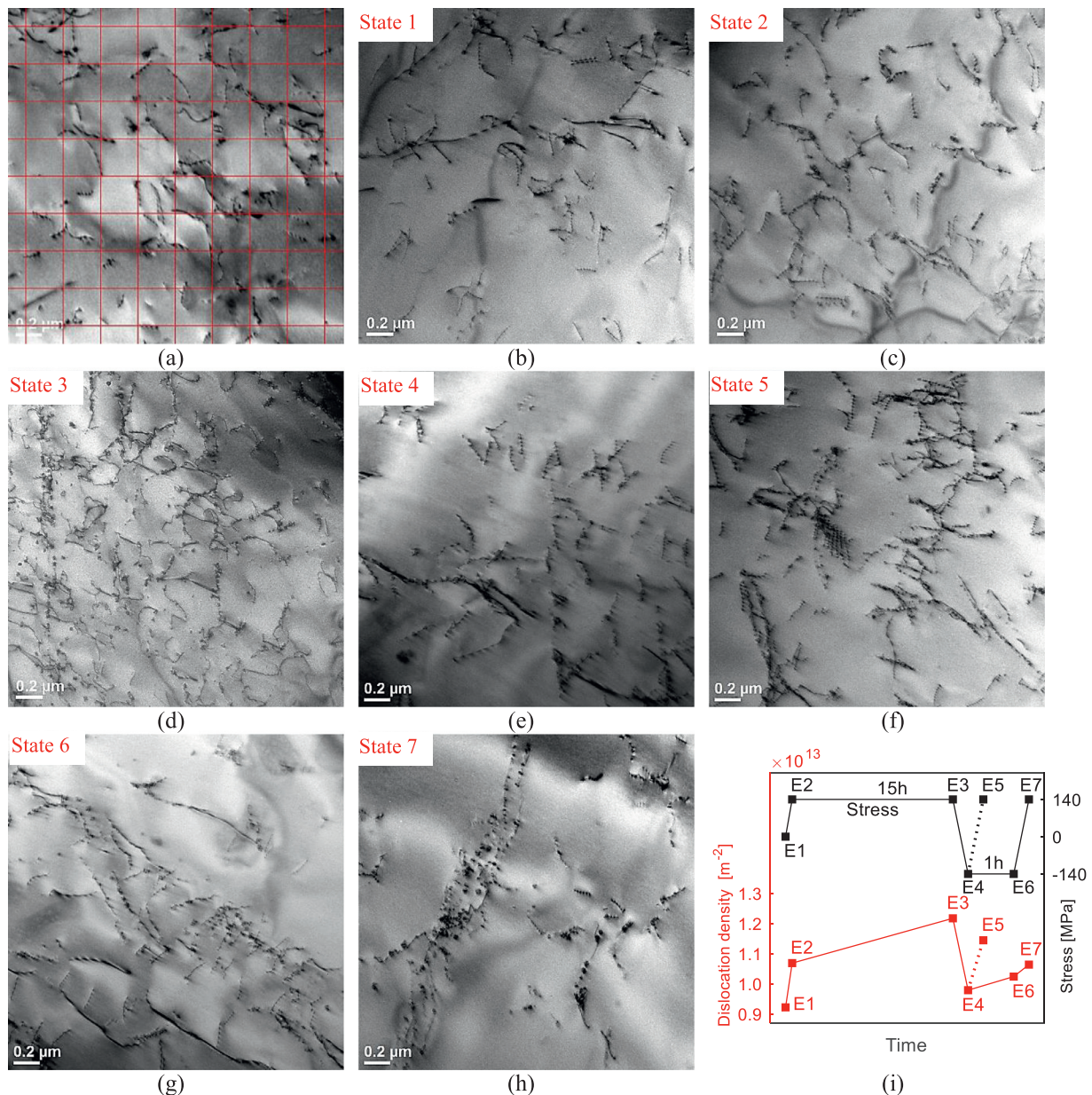


**Fig. 4.** An example of 'grid-intercept method' for calculation of dislocation density from TEM images (a). Examples of TEM BF images for states E1-E7 of the *ex-situ* experiment, respectively (b-h). TEM derived average dislocation density evolution for the *ex-situ* loading profile (i). All TEM images were taken using JEOL JEM2200fs at 200kV.

chrotron high energy XRD experiment was conducted to provide time-resolved evolution of dislocation density and internal lattice strain during stress-varying uniaxial creep loading. The *in-situ* experiment was conducted at beamline 1-ID of the Advanced Photon Source (APS), Argonne National Laboratory, USA. A monochromatic 71.676 keV X-ray beam with a  $150 \times 150 \mu\text{m}^2$  cross-section continuously illuminated the 316H sample gauge section (Fig. 6, inset) to generate *in-situ* diffraction data during the stress-varying creep test. Four GE-RT41 detectors were placed at a distance of 2 m from the sample to collect the Debye-Scherrer diffraction rings. The setup, testing procedure and details of diffraction data analysis to determine the dislocation density and lattice strain evolutions were identical to those comprehensively described in [12].

The examined loading profile for the *in-situ* experiment for 316H steel included different reverse-loading magnitudes and durations (Fig. 6). Under such conditions, various levels of PCR, from trivial for index I4 to very significant for index I14, were observed.

### Internal lattice strain

Fig. 7 presents the derived evolution of lattice strains for five crystallographic plane families of {111}, {200}, {220}, {311}, and {222} during the *in-situ* experiment; The calculated lattice strains include contributions from i) applied macroscopic load and ii) internal micro-level stresses/strains. The lattice strain contribution from the external stress was calculated using the lattice elastic moduli. The internal lattice strain evolution was accordingly derived, which can be interpreted as an indication of the internal stress. Similar to the internal lattice strain calculation from the ND examinations, only the lattice strain profile of the plane family with the largest variation, i.e. {200}, was further evaluated. Fig. 8 implies that the internal lattice strain formed and increased during the forward-loading (I2), and dropped upon unloading (I3). Reverse-loading (I5) further reduced the internal lattice strain and led to internal lattice strains with the opposite direction/sign to the one previously formed. The internal lattice strain reduction



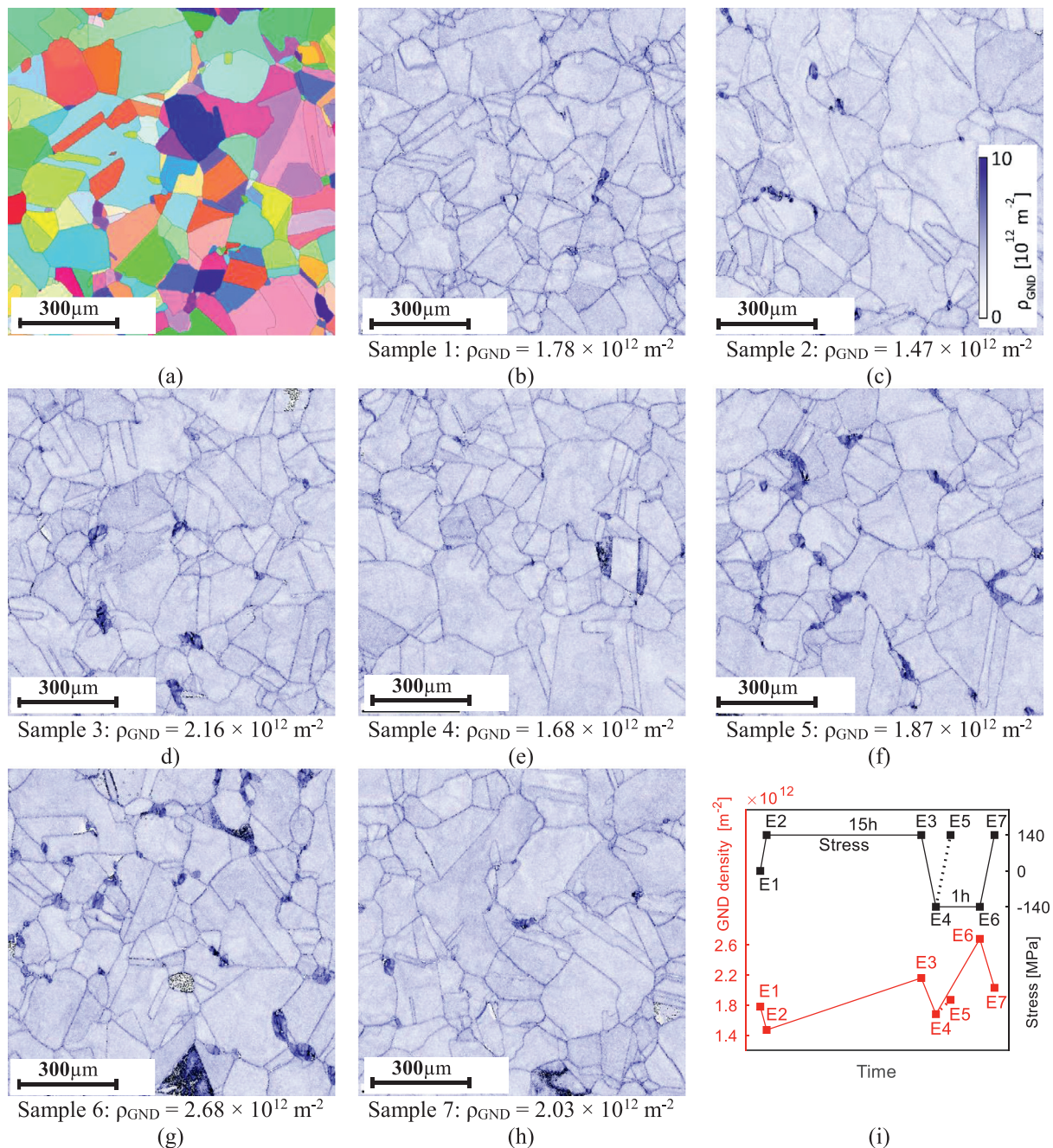


**Fig. 5.** An example of the inverse pole figure for state E1 (a). GND density maps for the samples of the *ex-situ* experiment (b-h; black colour corresponds to the dislocation density higher than  $1 \times 10^{13} \text{ m}^{-2}$ ) and evolution of GND density during the *ex-situ* experiment (i).\*

\*EBSD measurements were carried out using a Tescan Mira scanning electron microscope (SEM) equipped with Edax DigiView camera and OIM Analysis v.7 software. An electron beam of 20 kV, 16 nA was used for the orientation mapping, which was performed on a large ( $1 \text{ mm}^2$ ) area with a step size of  $2 \text{ }\mu\text{m}$  and  $8 \times 8$  diffraction pattern binning.

was significant for longer reverse-loading durations (I9 vs I11) and larger reverse-loading magnitudes (I9 vs I13).

#### Dislocation density

The CMWP method was employed to analyse the synchrotron high energy XRD data and estimate dislocation density evolution during the *in-situ* experiment. Fig. 9 indicates that unloading and reverse-loading often reduced the dislocation density. Interestingly, an increasing trend was observed during reverse-loading under high compressive stresses (index I13). The observed evolution trends for dislocation density and internal lattice strain from the *in-situ* experiments are generally consistent with the outcomes of the *ex-situ* experiments, which indicates the reliability of the ex-

perimental observations from the *ex-situ* experiments. Next section discusses the experimental evidence from the *in-situ* and *ex-situ* experiments, and provides a mechanistic explanation for the PCR phenomenon.

### 3. Discussion

Creep strain accumulation kinetics is controlled by dislocation movement, which is in turn governed by the applied (resolved shear) stress, internal stresses and material intrinsic resistance against dislocation movement (friction stress).

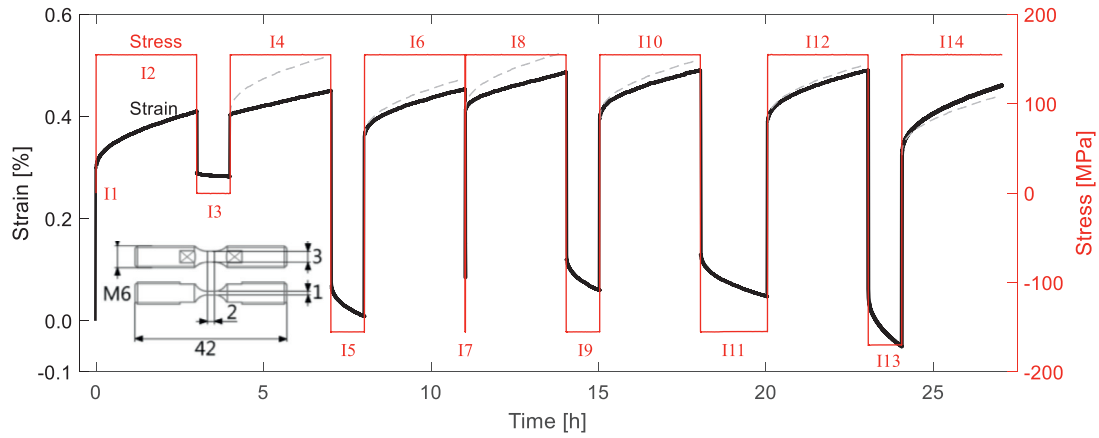


**Fig. 6.** Loading profile and strain accumulation response of 316H steel for the *in-situ* experiment. The corresponding primary creep profile (grey dotted line) is illustrated after each forward loading segment to show the extent of PCR activation.<sup>†</sup>

<sup>†</sup>To facilitate referring to and discussing the experimental observations, 14 indices are defined. I1: before the start of loading; I2: 155MPa/3h; I3: 0MPa/1h; I4: 155MPa/3h; I5: -155MPa/1h; I6: 155MPa/3h; I7: -155MPa/0h; I8: 155MPa/3h; I9: -155MPa/1h; I10: 155MPa/3h; I11: -155MPa/2h; I12: 155MPa/3h; I13: -170MPa/1h; I14: 155MPa/3h.

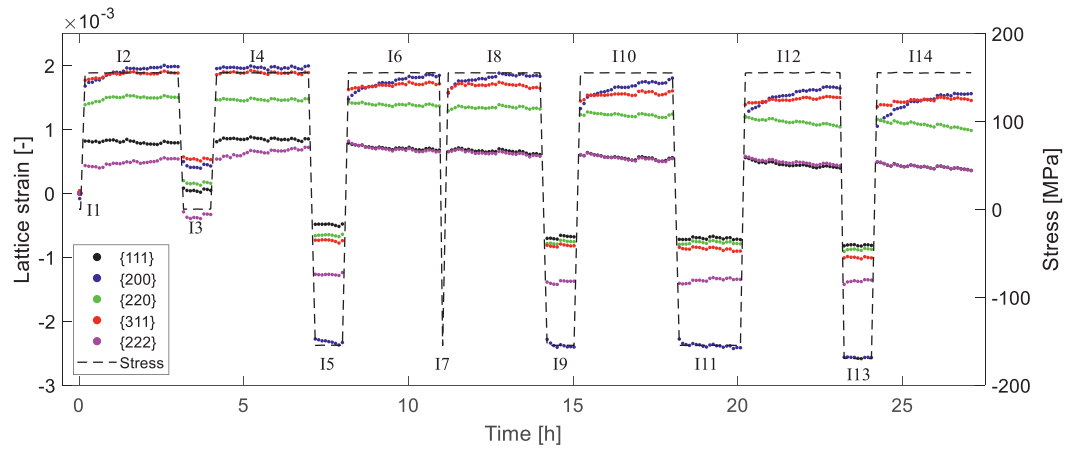


**Fig. 7.** Lattice strains evolution during the *in-situ* experiment.

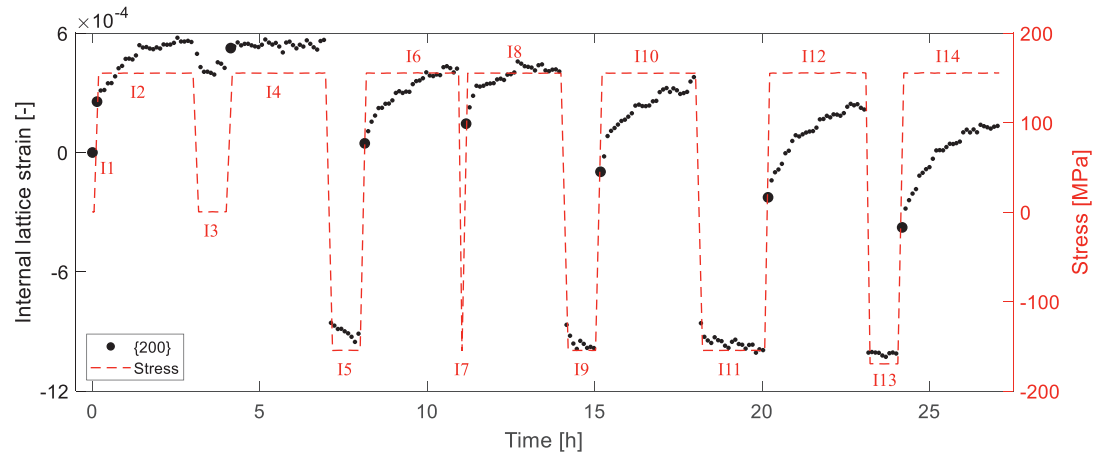


**Fig. 8.** Internal lattice strain evolution for {200} crystallographic plane family during the *in-situ* experiment (lattice elastic modulus of  $E_{200} = 109$  GPa [13] was considered for calculation of internal lattice strains).

During constant-stress creep loading, the formation of dislocation pileups (Fig. 10a), the bowing of dislocation-lines (Fig. 10b) and the development of inhomogeneous micro-strain fields (Fig. 10c) induce internal stresses against the applied stress and reduce the 'effective stress' acting on the dislocations. Therefore the creep strain rates decrease during the primary creep stage (Fig. 6: index I2). During reverse-loading, the pre-existing internal stress

fields partially or entirely relax (Fig. 8: index I5 and Figs. 2b, 5i: E3→E4) such that the creep rate upon reloading is higher than that before the reverse-loading (i.e. PCR, e.g. Fig. 6 index I6). New internal stress fields might form during reverse-loading to high-stress magnitudes and/or for long-durations (Fig. 8: indexes I11 and I13). Upon reloading, these new stress fields favour the applied stress and therefore creep rates even higher than those for

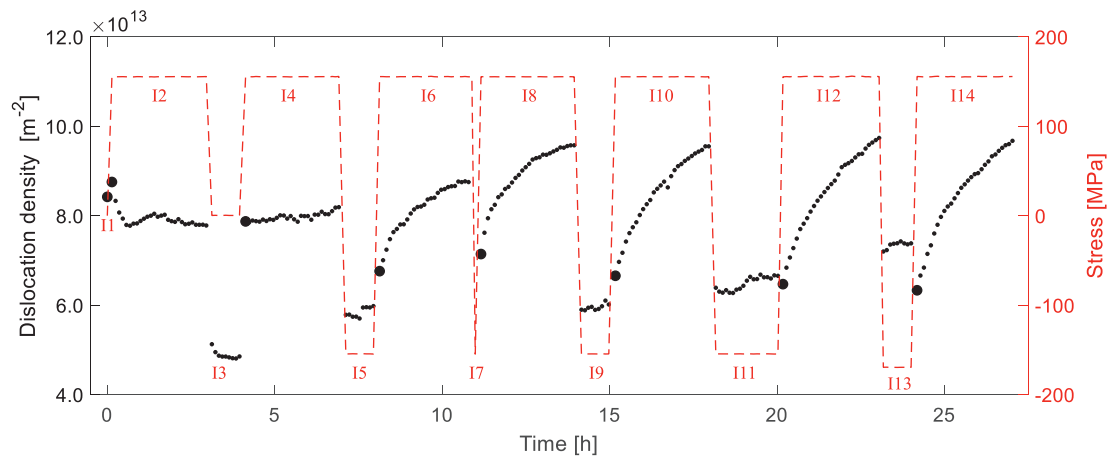


**Fig. 9.** CMWP calculated dislocation density evolution during the *in-situ* experiment. Peak broadening information from planes with large indices, i.e. {311}, {400}, {331} and {420}, were analysed by the CMWP method.

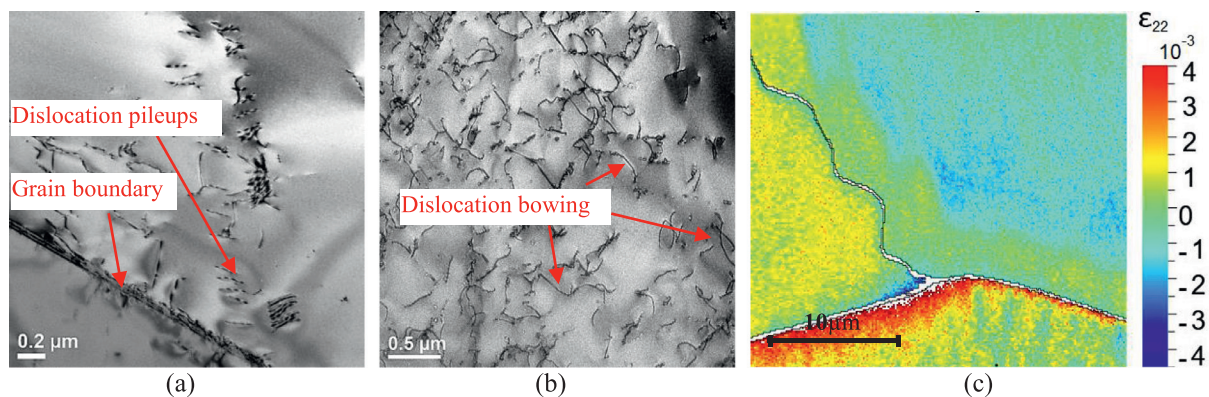


**Fig. 10.** TEM image and high (angular) resolution EBSD (HR-EBSD) map: Observation of the dislocation pileups close to a grain boundary (a), dislocation bowing (b) and elastic strain distribution (c). It should be noted that the apparent dislocation density and length in (b) are functions of the TEM foil thickness.<sup>‡</sup>

<sup>‡</sup>The elastic strain map in (c) was calculated from the diffraction pattern image cross-correlation based HR-EBSD evaluation. HR-EBSD evaluation was carried out with BLG Vantage CrossCourt v4 software. Points of the map were firstly filtered (confidence index > 0.2) based on the orientation indexation quality, excluding the points belonging to the grain boundaries. Then a reference pattern was assigned to each grain, which means all strain values are relative to the strain state of these 3 references. 20 regions of interest (128 pixel × 128 pixel) on all diffraction patterns were used and filtered through high and low pass FFT filters to reduce the noise of the calculation.

the early primary creep stage might be observed (i.e. significant PCR, e.g. Fig. 6: I14). The extent of PCR activation is proportional to the magnitude and duration of reverse-loading; i.e. negligible PCR was observed for index I4, partial PCR for index I6 and very significant PCR for index I14 were observed in Fig. 6.

The friction stress is another crucial parameter governing dislocation movement kinetics and hence the PCR phenomenon. Dislocation obstacles such as dislocations themselves, solute atoms, precipitates and grain boundaries increase the resistance against dislocation movement. For negligible variation in the grain size, solute atoms and precipitates, the friction stress is governed by the dislocation density [28]. Reverse-loading leads to the back movement of dislocations from pileups and the unbowing of dislocation-lines [29–31]. The back-moving dislocations might be annihilated by meeting other back-moving dislocations of the opposite sign on the same slip plane, leading to a reduction in the dislocation density (Fig. 9: I4→I5, and Figs 3 and 4i: E3→E4). Similarly, the unbowing mechanism shortens the dislocation-lines and therefore reduces the dislocation density. The reduction in dislocation density decreases the friction stress and results in high creep rates upon reloading (compared to those before the reverse-loading, e.g. Fig. 6: index I10). It should be noted that for long-duration reverse-loading at high-stress magnitudes, after the initial drop, a subsequent increase in the dislocation density is expected due to a significant activity of dislocation generation mechanisms, the forma-

tion of new dislocation pileups and the re-bowing of dislocation-lines (Fig. 9: indexes I11 and I13, and Figs. 3 and 4i: E3→E4→E6). Fig. 11 provides a schematic for the influence of reverse-loading on the dislocation structure and the expected extent of PCR.

In summary, for moderate reverse-loading, the relaxation of internal stress fields and the reduction of dislocation density allow easy movement of the mobile dislocations upon reloading and therefore, result in a period of high creep strain rate (i.e. PCR). For long-duration reverse-loading at high-stress magnitudes, the development of new internal stress fields contributes to increased effective stress for the movement of dislocations upon reloading and therefore leads to creep rates being even higher than the original primary creep rates.

#### 4. Dislocation-based model

The previous section provided a mechanistic explanation for the PCR phenomenon based on the dislocation structure evolution during stress-varying creep loading. In order to evaluate the validity of the proposed mechanisms and rationalise the gathered experimental observations, this section describes a corresponding dislocation-based model formulation.

Dislocation-based models have been developed over the past decades for describing the deformation behaviour of materials. Kocks and Mecking [32] proposed a one-internal variable model,



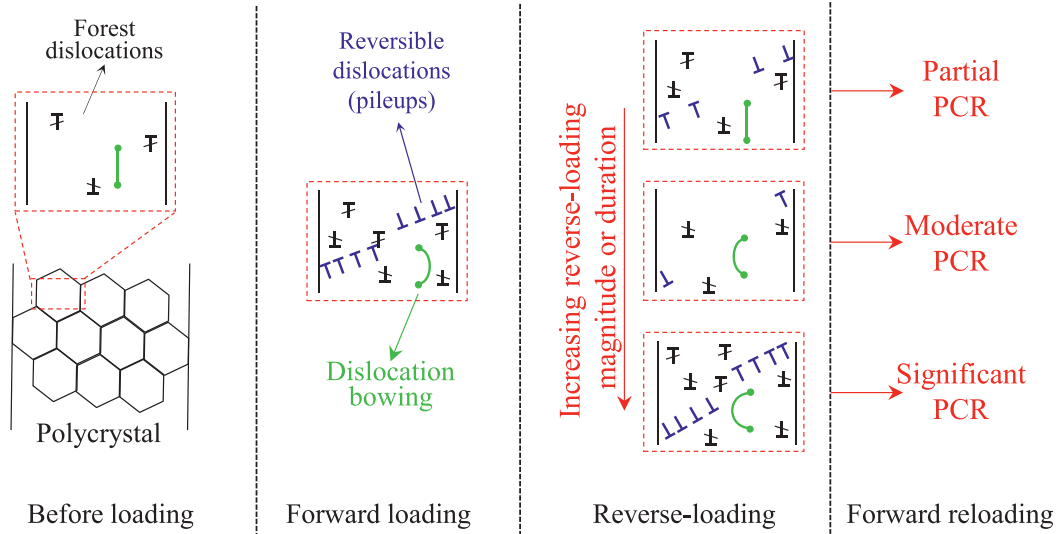


**Fig. 11.** Schematic illustration for describing the effect of reverse-loading conditions on the evolution of dislocation structure and the expected PCR extent upon reloading.

which uses the evolution of average dislocation density to describe the material deformation behaviour of alloys under steady state loading conditions [33]. Later, several studies [34–38] extended the Kocks-Mecking model by employing multiple-internal variables for representing the stress-strain response of materials during cyclic loading scenarios. Following [36–38], the present study divides dislocations into two categories of reversible and forest (irreversible) dislocations (i.e. a two-internal variable model). Reversible dislocations are assumed to accumulate in front of dislocation obstacles and form pileups and therefore move back and possibly annihilate upon a strain path reversal [29,30,36–38]. On the other hand, forest dislocations are permanently immobilised due to interaction with dislocation barriers, and hence their evolution does not directly depend on the deformation path [36–38]. Additionally, the model takes into account the contribution of dislocation-line bowing towards dislocation density and strain development [39,40].

Employment of dislocation-based formulations for representing the macroscopic response of polycrystals requires consideration of a crystal plasticity model. Different crystal plasticity modelling frameworks have been proposed; namely Taylor [37,41], self-consistent [5,8] and finite element based crystal plasticity [6,42]. In this study, for the sake of simplicity, a Taylor factor was used to describe the relationship between strain/stress state in slip-system and macroscopic scales. It should be noted that this model does not take into account deformation inhomogeneity between grains, and therefore employment of a more sophisticated crystal plasticity framework (e.g. self-consistent) is beneficial. Based on the Taylor factor  $M$  (3.06 for FCC polycrystals [43]), the micro-scale (slip-system level) resolved shear stress and strain rate ( $\tau$  and  $\dot{\gamma}$ ) are given as:

$$\tau = \sigma / M \quad (3)$$

$$\dot{\epsilon}_{in} = \frac{\dot{\gamma}}{M} \quad (4)$$

where  $\sigma$  and  $\dot{\epsilon}_{in}$  are the (von Mises, here identical to axial) macroscopic stress and inelastic strain rate, respectively. It is assumed that the resolved shear strain rate includes contributions from dislocation gliding and bowing:

$$\dot{\gamma} = \dot{\gamma}_g + \dot{\gamma}_b \quad (5)$$

A power-law equation [5,7,44,45] is employed for defining resolved shear strain rate as a function of resolved shear stress, intrinsic dislocation movement resistance (friction stress,  $\tau_{fric}$ ), and

internal stress,  $\tau_{int}$ :

$$\dot{\gamma}_g = A \left| \frac{\tau - \tau_{int}}{\tau_{fric}} \right|^n \text{sign}(\tau - \tau_{int}) \quad (6)$$

where  $A$  and  $n$  are material model constants. The friction and internal stresses are assumed to be related to the population of total and reversible dislocations, respectively [36–38].

$$\tau_{fric} = \alpha_{fric} \mu b \sqrt{\rho_{for} + L_{rev} |\rho_{rev}| + L_{bow} |\rho_{bow}|} \quad (7)$$

$$\tau_{int} = \alpha_{int} \mu b \sqrt{|\rho_{rev}|} \text{sign}(\rho_{rev}) \quad (8)$$

where  $\alpha_{fric}$ ,  $\alpha_{int}$ ,  $L_{rev}$  and  $L_{bow}$  are material model constants which depend on the strength of the interactions between dislocations;  $\mu$  is the shear modulus;  $b$  is the magnitude of the Burgers vector;  $\rho_{for}$  and  $\rho_{rev}$  are densities of the forest and reversible dislocations, and  $\rho_{bow}$  is the contribution of dislocation-line bowing to the total dislocation density. It should be noted that the sign of reversible dislocations (and bowed dislocations) corresponds to the direction of shear strain under which they were generated.

Similar to [5,35–38,41], the present model considers three mechanisms of dislocation generation, dynamic and static recovery to govern the evolution for forest and reversible dislocation densities. It should be noted that the ratio of forest and reversible dislocations is not fixed and varies during the course of deformation, depending on the loading path, e.g. a reverse loading significantly decreases the density of reversible dislocations while the forest dislocation density might even increase. Therefore and similar to [36–38], two different evolution equations were employed for calculating the evolution of the forest and reversible dislocations:

$$\dot{\rho}_{for} = (1 - p) \frac{|\dot{\gamma}_g|}{bd} - R_{for} \rho_{for} |\dot{\gamma}_g| - r_{for} \rho_{for} \quad \rho_{for}|_{t=0} = \rho_0 \quad (9)$$

$$\dot{\rho}_{rev} = p \frac{\dot{\gamma}_g}{bd} - R_{rev} \rho_{rev} |\dot{\gamma}_g| - r_{rev} \rho_{rev} \quad \rho_{rev}|_{t=0} = 0 \quad (10)$$

where  $R_{for}$ ,  $R_{rev}$ ,  $r_{for}$  and  $r_{rev}$  are material model constants which are expected to increase with temperature, and  $\rho_0$  is the initial dislocation density. Parameter  $p$  is the fraction of reversible dislocations among all the generated dislocations [37], which is assumed to follow  $p = p_1 + p_2 \dot{\gamma}_g$ . The dislocation mean free path  $d$  can be calculated as [36]:

$$\frac{1}{d} = \frac{\sqrt{\rho_{for} + |\rho_{rev}| + |\rho_{bow}|}}{K} + \frac{1}{D} \quad (11)$$



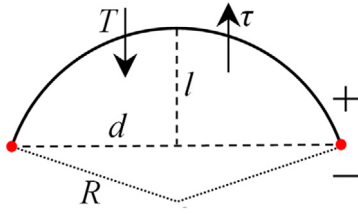


**Fig. 12.** Schematic illustration of dislocation bowing. The sign of  $R$  and  $l$  indicates the bowing direction.

where  $D$  is the average grain size, and  $K$  is a material model constant [38].

The formulation for consideration of the dislocation bowing mechanism is derived as follows. As shown in Fig. 12, a bowed dislocation-line is intrinsically under tension  $T$  to straighten and shorten [39]:

$$T = \frac{\mu b}{2R} \quad (12)$$

where  $R$  is the radius of dislocation bow. For resolved shear stresses ( $\tau$ ) larger or smaller than  $T$ , the dislocation-line further bows or straightens, respectively. Therefore, the driving force for the change in the dislocation bow's state is given by  $\tau_{eff} = \tau - T$  and the dislocation glide velocity is given by [46]:

$$\begin{aligned} v &= \lambda v_0 \exp\left(-\frac{Q}{k_B T}\right) \sinh\left(\frac{V}{k_B T} |\tau_{eff}|\right) \text{sign}(\tau_{eff}) \\ &= \lambda' \sinh(V' |\tau_{eff}|) \text{sign}(\tau_{eff}) \end{aligned} \quad (13)$$

where  $\lambda$  is the jump width;  $v_0$  is the attack frequency;  $Q$  is the effective activation energy for dislocation glide;  $k_B$  is the Boltzmann constant;  $V$  and  $T$  are the activation volume and temperature, respectively. Therefore, the position of the centre point of the dislocation-line can be incrementally determined as  $l = l^{-1} + v \Delta t$ . Assuming that both reversible and forest dislocations contribute to the bowing mechanism, it can be stated that [46]:

$$\gamma_b = (\rho_{for} + |\rho_{rev}|) b \frac{S}{d} \text{sign}(R) \quad (14)$$

$$\rho_{bow} = \left( \frac{2|R| \arcsin\left(\frac{d}{2|R|}\right)}{d} - 1 \right) (\rho_{for} + |\rho_{rev}|) \text{sign}(R) \quad (15)$$

where  $R$  and  $S$  are the radius and the swept area by the dislocation bow, given by:

$$R = \frac{l^2 + \left(\frac{d}{2}\right)^2}{2l} \quad (16)$$

$$S = R^2 \arcsin\left(\frac{d}{2|R|}\right) - d/4 \sqrt{(4R^2 - d^2)} \quad (17)$$

For a given macroscopic stress profile, the presented model describes the strain accumulation and evolution of dislocation structure and internal stress state in the alloy. The above equations have been implemented into a Matlab® script where an explicit-integration scheme was used to integrate the system of equations (supplementary materials). The model was calibrated based on the experimental observations from the *in-situ* experiment, and the derived model parameters are summarised in Table 1. Cross-checks were performed to compare the derived model parameters with the other works. For example, the obtained material model constants  $\alpha_{rev} = 0.318$  and  $\alpha_{for} = 0.511$  are comparable with the reported values 0.35 in [47,48] and 0.5 in [37,38]. On the other hand,

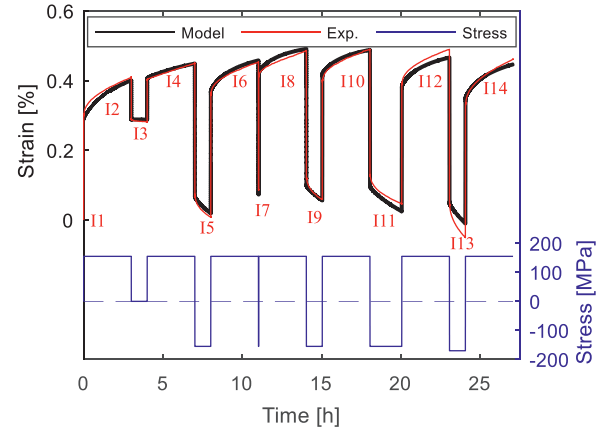


**Fig. 13.** Comparison of the experimental and model represented strain evolution during the *in-situ* experiment.

the calculated parameters for the dynamic recovery at 650°C in our model are  $R_{for} = 825$  and  $R_{rev} = 402$  which are much larger than the values in [5,6] for 316H steel at 550°C ( $\sim 8$ ). The larger recovery coefficients in the present study, at least partially, are related to the higher examined temperature (i.e. 650 vs 550°C). Figs. 13–15 compare the experimental and model presented evolution of strain, dislocation density and internal stress/strain during both *in-situ* and *ex-situ* experiments. It should be noted that, as the validity of dislocation density measurement techniques is limited to representing the evolution trends, the dislocation density quantities resulting from the proposed model could not be directly validated.

In agreement with the experimental observations, the model expects a more significant PCR after reverse-loading to larger reverse-loading magnitudes and for longer durations (Fig. 13).

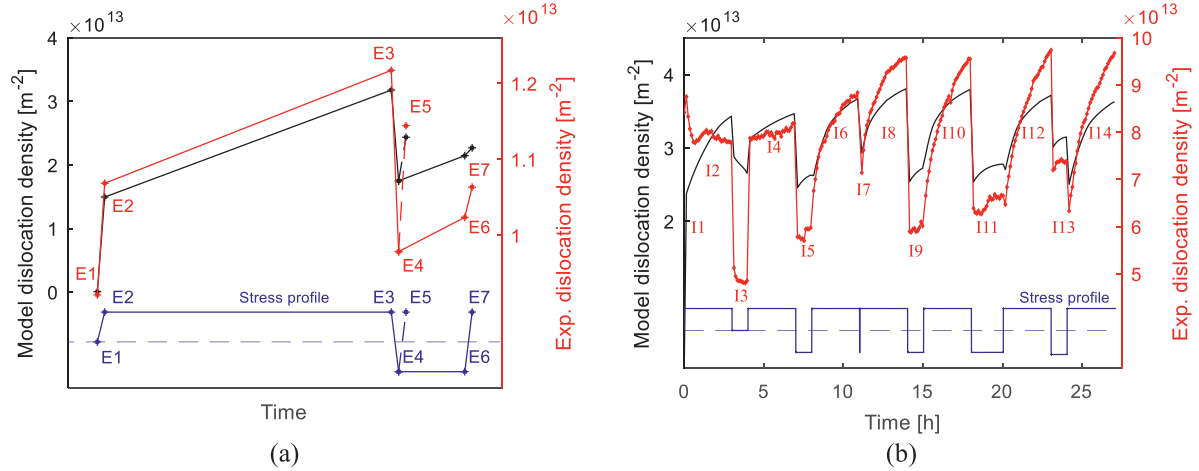
Fig. 14 compares the experimental and model presented evolution trends for dislocation density during the *in-situ* and *ex-situ* experiments which indicates an acceptable level of consistency. The model could describe the experimentally observed dislocation density evolution during the reverse-loadings and expects a lower dislocation density after stress-transients to larger reverse-loading magnitudes and for longer reverse-loading durations. Such a lower dislocation density accounts for the observed significant PCR upon reloading for such cases in Fig. 13 (indexes I12 and I14). It is worthy to note that the reduction in dislocation density during reverse-loading could not be explained based on the previously developed model by Petkov et al. [5] for the 316H alloy. Interestingly and consistent with the experimental records, upon reloading, the model anticipates an increase in the dislocation density after short-duration reverse-loading at low-stress magnitudes (e.g. I5→I6 and I9→I10) and a decrease in the dislocation density after long-duration reverse-loading at high-stress magnitudes (e.g. I11→I12 and I13→I14). A discrepancy between the model and experimental dislocation densities was observed during the first few hours of the *in-situ* test which might originate from the unknown prior-loading history of the ex-service 316H alloy.

Fig. 15 demonstrates that the model representations for internal stress evolution agree with the experimentally measured internal strains during the *ex-situ* and *in-situ* experiments. The model expects that the internal stress is smaller after stress-transients to larger reverse-loading magnitudes and longer reverse-loading durations which explains the observed significant PCR upon reloading for such cases in Fig. 13.

The acceptable consistency between the experimental observations and model descriptions in Figs. 13–15 demonstrates the reliability of the proposed mechanistic explanation and the developed

**Table 1**  
Obtained model parameters for the 316H steel at 650°C.

Parameter	Value	Unit	Parameter	Value	Unit	Parameter	Value	Unit
$E$	$1.48 \times 10^2$	GPa	$L_{bow}$	$1.23 \times 10^{-2}$	-	$R_{for}$	$8.25 \times 10^2$	-
$A$	$1.15 \times 10^{-20}$	1/s	$\rho_0$	$7.93 \times 10^{10}$	$m^{-2}$	$R_{rev}$	$4.02 \times 10^2$	-
$n$	$7.98 \times 10^1$	-	$u$	$5.69 \times 10^1$	GPa	$r_{for}$	$3.06 \times 10^{-4}$	1/s
$\alpha_{for}$	$5.11 \times 10^{-1}$	-	$K$	$1.06 \times 10^0$	-	$r_{rev}$	$4.31 \times 10^{-6}$	1/s
$\alpha_{rev}$	$3.18 \times 10^{-1}$	-	$p_1$	$1.66 \times 10^{-1}$	-	$\lambda'$	$1.02 \times 10^{-19}$	m/s
$L_{rev}$	$1.47 \times 10^{-1}$	-	$p_2$	$6.26 \times 10^1$	-	$V'$	$1.40 \times 10^{-6}$	1/Pa



**Fig. 14.** Comparison of the experimental and model representations for the evolution of dislocation density during the *ex-situ* (a) and *in-situ* (b) studies. The dislocation density values in (a) and (b) are derived from TEM and XRD analyses (Figs. 4i, 9), respectively.

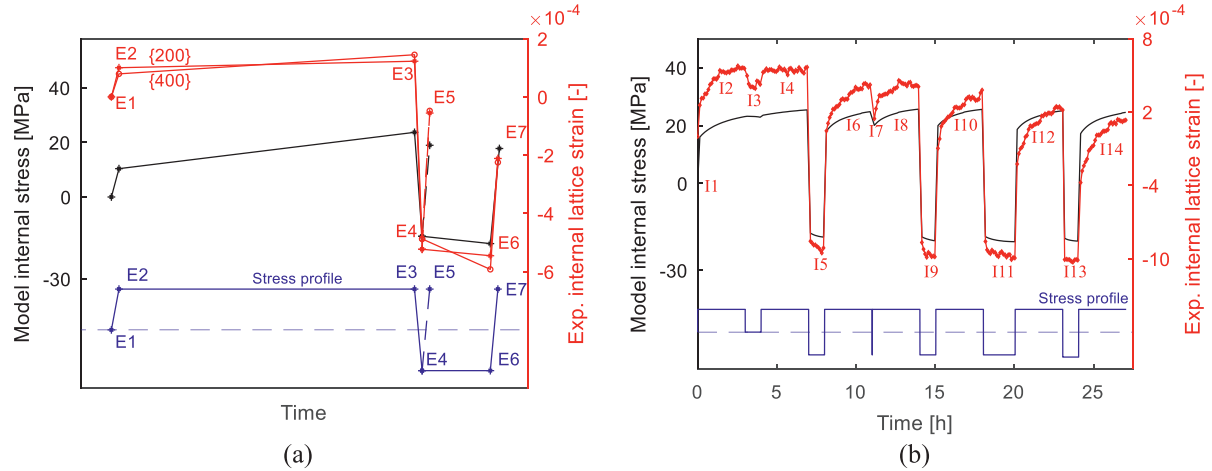


**Fig. 15.** Comparison of the experimental and model representations for the evolution of internal lattice strain/stress during the *ex-situ* (a) and *in-situ* (b) studies.

dislocation-based model for describing the PCR behaviour of 316H alloy at 650°C.

## 5. Concluding Remarks

The evolution of creep strain and microstructure in 316H stainless steel during stress-varying creep loading conditions at 650°C has been investigated. Periods of accelerated creep, i.e. regeneration of the primary creep stage or PCR, are observed upon reloading after stress reversals. The extent of the acceleration is proportional to the magnitude and duration of the reverse stress. Observations from different microstructural investigation techniques, including *in-situ* synchrotron high energy X-ray diffraction, neutron diffraction, transmission electron microscopy, and electron backscatter diffraction analysis, reveal a correlation between the

extent of PCR activation and the evolution of dislocation density and internal stress state of the material during stress reversals. Interpretation of the microstructural data suggests that the formation/relaxation of dislocation pileups and the bowing/unbowing of dislocation-lines are the responsible mechanisms for the PCR phenomenon. The gained mechanistic understanding has then been used to develop a mathematical formulation for representing the evolution of creep strain, dislocation density and internal stress state of the alloy during stress-varying creep loading conditions. The model considers forest and reversible dislocation densities to track the evolution of friction and internal stresses which affect dislocation kinetics and the material's deformation response. In addition, a model formulation has been developed to take into account the contribution of dislocation-line bowing to strain and dislocation density development during stress-varying creep condi-

tions. Ultimately, the effectiveness of the developed dislocation-based model and therefore the reliability of the proposed mechanistic explanation for the PCR phenomenon has been demonstrated by the successful representation of the strain and microstructure evolution of 316H alloy during the conducted *in-situ* and *ex-situ* experiments at 650°C.

#### Supplementary materials

The supplementary data provides a Matlab® script that numerically integrates the developed material model formulation and creates the graphs presented in Figs. 13–15.

#### Data availability

All raw/processed data necessary for reproducing results in this study can be accessed on reasonable request.

#### Declaration of Competing Interest

The authors declare that they have no known competing financial interests or personal relationships that could have appeared to influence the work reported in this paper.

#### Acknowledgments

Financial support by the Swiss National Science Foundation (SNSF; grant number 169877) is gratefully acknowledged. SK was supported by the EMPAPOSTDOCS-II programme, that has received funding from the European Union's Horizon 2020 research and innovation programme under the Marie Skłodowska-Curie grant agreement number 754364. The authors are grateful to Dr. M.P. Petkov and Dr. J. Hu for their support for the development of dislocation-based model. This research used resources of the Advanced Photon Source, a U.S. Department of Energy (DOE) Office of Science User Facility operated for the DOE Office of Science by Argonne National Laboratory under Contract No. DE-AC02-06CH11357. The authors are grateful to STFC for awarding neutron beamtime at the ISIS facility (UK), and the assistance of Dr. S. Kabra.

#### Supplementary materials

Supplementary material associated with this article can be found, in the online version, at doi:10.1016/j.actamat.2021.117130.

#### Reference

- [1] X. Li, S. Holdsworth, E. Mazza, E. Hosseini, Creep behaviour of AISI 316H stainless steel under stress-varying creep loading conditions: primary creep regeneration, *Mater. High Temp.* 36 (3) (2019) 240–252.
- [2] X. Li, S. Holdsworth, E. Mazza, E. Hosseini, Creep behaviour of a high chromium martensitic steel under stress varying creep loading conditions: primary creep regeneration (PCR), *Int. J. Press. Vessels Pip.* (2020) 104188.
- [3] X. Li, S. Holdsworth, E. Mazza, E. Hosseini, Comparison of primary creep regeneration and anelastic recovery behaviour of 316H austenitic and 10%Cr martensitic steel, *Mech. Mater.* (2020) 103474.
- [4] A. Al Mamun, C. Simpson, D. Agius, T.L. Lee, S. Kabra, C. Truman, M. Mostafavi, D. Knowles, A novel insight into the primary creep regeneration behaviour of a polycrystalline material at high-temperature using *in-situ* neutron diffraction, *Materials Sci. Engineering: A* (2020) 139374.
- [5] M.P. Petkov, J. Hu, A.C. Cocks, Self-consistent modelling of cyclic loading and relaxation in austenitic 316H stainless steel, *Philos. Mag.* 99 (7) (2019) 789–834.
- [6] M.P. Petkov, J. Hu, E. Tarleton, A.C. Cocks, Comparison of self-consistent and crystal plasticity FE approaches for modelling the high-temperature deformation of 316H austenitic stainless steel, *Int. J. Solids Struct.* 171 (2019) 54–80.
- [7] J. Hu, B. Chen, D.J. Smith, P.E. Flewitt, A.C. Cocks, Self-consistent modelling and the evaluation of lattice deformation in a polycrystalline austenitic stainless steel, *Mater. Today: Proc.* (2015) 424–433.
- [8] J. Hu, A.C. Cocks, A multi-scale self-consistent model describing the lattice deformation in austenitic stainless steels, *Int. J. Solids Struct.* 78 (2016) 21–37.
- [9] B. Chen, J.N. Hu, P.E. Flewitt, A.C.F. Cocks, R.A. Ainsworth, D.J. Smith, D.W. Dean, F. Scenini, Effect of thermal ageing on creep and oxidation behaviour of Type 316H stainless steel, *Mater. High Temp.* 32 (6) (2015) 592–606.
- [10] A. Mamun, R.J. Moat, A. J. Kelleher, P.J. Bouchard, Generation of intergranular strains during high temperature creep fatigue loading of 316H stainless steel, *Mater. High Temp.* 31 (4) (2014) 378–382.
- [11] A. Al Mamun, R.J. Moat, P.J. Bouchard, Origin and effect of back stress on cyclic creep deformation of 316H stainless steel, in: *Proceedings of the ASME Pressure Vessels and Piping Conference - 2015*, 5, 2015.
- [12] X. Li, S.R. Holdsworth, S. Kalácska, L. Balogh, J.-S. Park, A.S. Sologubenko, X. Maeder, S. Kabra, E. Mazza, E. Hosseini, Primary creep regeneration in 10%Cr martensitic steel: *in-situ* and *ex-situ* microstructure studies, *Mater. Design* (2020) 109405.
- [13] A. Rao, P. John Bouchard, S.M. Northover, M.E. Fitzpatrick, Anelasticity in austenitic stainless steel, *Acta Mater.* 60 (19) (2012) 6851–6861.
- [14] G. Ribárik, T. Ungár, J. Gubicza, MWP-fit: a program for multiple whole-profile fitting of diffraction peak profiles by *ab initio* theoretical functions, *J. Appl. Crystallogr.* 34 (5) (2001) 669–676.
- [15] G. Ribárik, J. Gubicza, T. Ungár, Correlation between strength and microstructure of ball-milled Al–Mg alloys determined by X-ray diffraction, *Materials Sci Eng* 387 (2004) 343–347.
- [16] L. Balogh, G. Ribárik, T. Ungár, Stacking faults and twin boundaries in fcc crystals determined by x-ray diffraction profile analysis, *J. Appl. Phys.* 100 (2) (2006) 023512.
- [17] G. Ribárik, Modeling of Diffraction Patterns Based On Microstructural Properties, Eötvös Loránd University, 2008 Ph.D. Thesis.
- [18] L. Balogh, T. Ungár, Y. Zhao, Y. Zhu, Z. Horita, C. Xu, T.G. Langdon, Influence of stacking-fault energy on microstructural characteristics of ultrafine-grain copper and copper–zinc alloys, *Acta Mater.* 56 (4) (2008) 809–820.
- [19] M.V. Alvarez, J.R. Santisteban, P. Vizcaino, G. Ribárik, T. Ungar, Quantification of dislocations densities in zirconium hydride by X-ray line profile analysis, *Acta Mater.* 117 (2016) 1–12.
- [20] O. Muransky, L. Balogh, M. Tran, C. Hamelin, J.-S. Park, M.R. Daymond, On the measurement of dislocations and dislocation substructures using EBSD and HRSD techniques, *Acta Mater.* 175 (2019) 297–313.
- [21] Wilkens, M.I., Theoretical aspects of kinematical X-ray diffraction profiles from crystals containing dislocation distributions (Fourier transform of X ray diffraction line profiles from crystals with dislocations), *NBS Fundamental Aspects of Dislocation Theory*, 1970. 2.
- [22] T. Ungar, I. Dragomir, A. Revesz, A. Borbely, The contrast factors of dislocations in cubic crystals: the dislocation model of strain anisotropy in practice, *J. Appl. Crystallogr.* 32 (1999) 992–1002.
- [23] T. Ungár, L. Balogh, G. Ribárik, Defect-related physical-profile-based X-ray and neutron line profile analysis, *Mater. Trans. A* 41 (5) (2010) 1202–1209.
- [24] U. Martin, U. Muhle, H. Oettel, The quantitative measurement of dislocation density in the transmission electron microscope, *Prakt. Metallogr.* 32 (9) (1995) 467–476.
- [25] M.-S. Pham, FATIGUE BEHAVIOUR OF AISI 316L: Mechanical response, Microstructural evolution, Fatigue crack propagation, & Physically-based constitutive modelling, ETH Zurich, 2013.
- [26] D. Field, P. Trivedi, S. Wright, M. Kumar, Analysis of local orientation gradients in deformed single crystals, *Ultramicroscopy* 103 (1) (2005) 33–39.
- [27] P.J. Konijnenberg, S. Zaefferer, D. Raabe, Assessment of geometrically necessary dislocation levels derived by 3D EBSD, *Acta Mater.* 99 (2015) 402–414.
- [28] B. Chen, P.E.J. Flewitt, A.C.F. Cocks, D.J. Smith, A review of the changes of internal state related to high temperature creep of polycrystalline metals and alloys, *Int. Mater. Rev.* 60 (1) (2014) 1–29.
- [29] F. Mompou, D. Caillard, M. Legros, H. Mughrabi, In situ TEM observations of reverse dislocation motion upon unloading in tensile-deformed UFG aluminium, *Acta Mater.* 60 (8) (2012) 3402–3414.
- [30] S. Kondo, T. Mitsuoka, N. Shibata, Y. Ikuhara, Direct observation of individual dislocation interaction processes with grain boundaries, *Sci. Adv.* 2 (11) (2016).
- [31] L. Bueno, R. Bell, Anelastic creep behaviour of RR-58 aluminum alloy at 180°C: Phenomenological aspects and analysis based on the unbowing of dislocation segments, *Materials Sci. Engineering: A* 410 (2005) 72–78.
- [32] H. Mecking, U. Kocks, Kinetics of flow and strain-hardening, *Acta Metall.* 29 (11) (1981) 1865–1875.
- [33] Y. Estrin, H. Mecking, A unified phenomenological description of work hardening and creep based on one-parameter models, *Acta Metall.* 32 (1) (1984) 57–70.
- [34] Y. Estrin, H. Braasch, Y. Brechet, A dislocation density based constitutive model for cyclic deformation, *J. Eng. Mater. Technol.* 118 (4) (1996).
- [35] Y. Estrin, Dislocation theory based constitutive modelling: foundations and applications, *J. Mater. Process. Technol.* 80 (1998) 33–39.
- [36] W. Wen, M. Borodachenkova, C. Tomé, G. Vincze, E. Rauch, F. Barlat, J. Grácio, Mechanical behavior of Mg subjected to strain path changes: experiments and modeling, *Int. J. Plast.* 73 (2015) 171–183.
- [37] E. Rauch, J. Grácio, F. Barlat, G. Vincze, Modelling the plastic behaviour of metals under complex loading conditions, *Model. Simul. Mater. Sci. Eng.* 19 (3) (2011) 035009.
- [38] K. Kitayama, C. Tomé, E. Rauch, J. Grácio, F. Barlat, A crystallographic dislocation model for describing hardening of polycrystals during strain path changes. Application to low carbon steels, *Int. J. Plast.* 46 (2013) 54–69.
- [39] Z. Arechabaleta, P. van Liempt, J. Sietsma, Quantification of dislocation structures from anelastic deformation behaviour, *Acta Mater.* 115 (2016) 314–323.
- [40] M. Giordana, P.-F. Giroux, I. Alvarez-Armas, M. Sauzay, A. Armas, Micromechanical modeling of the cyclic softening of EUROFER 97 steel, *Procedia Eng.* 10 (2011) 1268–1273.



- [41] U. Kocks, H. Mecking, Physics and phenomenology of strain hardening: the FCC case, *Prog. Mater. Sci.* 48 (3) (2003) 171–273.
- [42] F. Roters, P. Eisenlohr, L. Hantcherli, D.D. Tjahjanto, T.R. Bieler, D. Raabe, Overview of constitutive laws, kinematics, homogenization and multiscale methods in crystal plasticity finite-element modeling: Theory, experiments, applications, *Acta Mater.* 58 (4) (2010) 1152–1211.
- [43] M. Kassner, K. Kyle, Taylor hardening in five power law creep of metals and class M alloys, in: *Nano and Microstructural Design of Advanced Materials*, Elsevier, 2003, pp. 255–271.
- [44] J.-L. Chaboche, A review of some plasticity and viscoplasticity constitutive theories, *Int. J. Plast.* 24 (10) (2008) 1642–1693.
- [45] J. Chaboche, D. Nouailhas, A unified constitutive model for cyclic viscoplasticity and its applications to various stainless steels, *J. Eng. Mater. Technol.* 111 (4) (1989) 424–430.
- [46] F. Roters, D. Raabe, G. Gottstein, Work hardening in heterogeneous alloys—a microstructural approach based on three internal state variables, *Acta Mater.* 48 (17) (2000) 4181–4189.
- [47] R. Madec, B. Devincre, L.P. Kubin, From dislocation junctions to forest hardening, *Phys. Rev. Lett.* 89 (25) (2002) 255508.
- [48] J. Hu, B. Chen, D.J. Smith, P.E. Flewitt, A.C. Cocks, On the evaluation of the Bauschinger effect in an austenitic stainless steel—The role of multi-scale residual stresses, *Int. J. Plast.* 84 (2016) 203–223.